an inverse correlation with hepatic glutathione content.

The present study had two advantages compared with the BSO study previously reported. First, the glutathione-depleting mechanism differs from phorone (a reactor to GSH thiol) and BSO (an inhibitor of gamma-glutamylcysteine synthetase). Comparing the two glutathione-depleting mechanisms, the phorone-induced one is thought to be more similar to drug-induced glutathione depletion (as in the acetaminophen overdose-induced one) where hepatic glutathione is depleted by elevated elimination, not by inhibition of glutathione synthesis. Second, the present study set multiple dose ranges and time points. The total number of rats tested in the phorone study was 36 (twelve 400 mg/kg phorone-treated rats were excluded from the gene selection procedure), whereas the previous BSO study used only 8 rats (Kiyosawa *et al.*, 2004). Thus, the GSH probe sets identified in the present study would give us more reliable information for evaluation of the potential risk of drug-induced glutathione depletion.

The GSH probe sets contained antioxidant/phase II drug-metabolizing enzymes, oxidative stress markers, transporters, metabolism-related genes, transcription factors and signal transduction-related genes, and others. GSH probe sets contain a modifier subunit of glutamate cysteine ligase gene, which encodes a key enzyme for glutathione synthesis (Moinova and Mulcahy, 1999). In addition, a prototypical oxidative stress-responsive gene, heme oxygenase I, which is reported to be regulated by oxidative stress sensor Nrf2 (Nguyen *et al.*, 2003), was identified as GSH probe sets. Furthermore, several genes were found to be in common with previously reported gene sets identified from the BSO-induced glutathione depletion model rat, such as GTP cyclohydrolase I and HMG-CoA reductase (Kiyosawa *et al.*, 2004). On the other hand, a

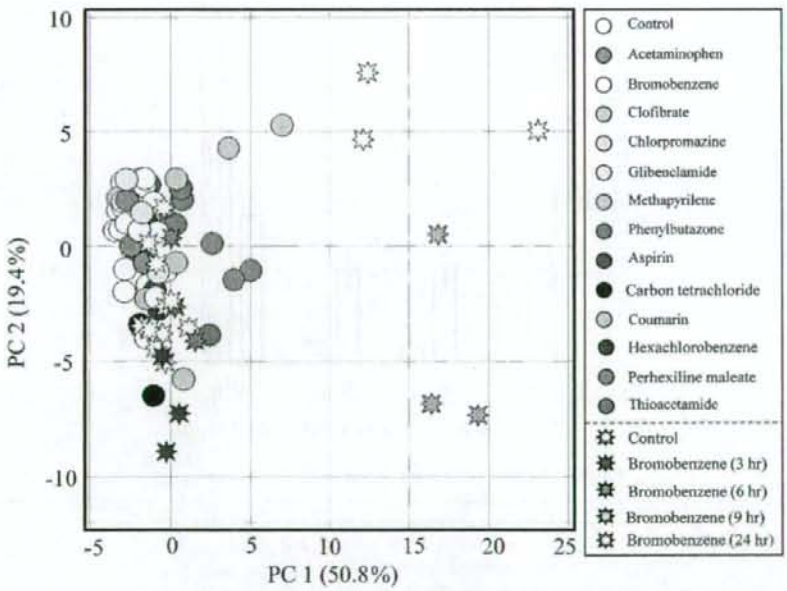

Fig. 6. Time-course of gene expression profile in rat liver treated with bromobenzene.
PCA was performed using GSH probe sets for GeneChip data of rat livers 3, 6, 9 and 24 hr after 300 mg/kg bromobenzene treatment, as well as those 24 hr after treatment with hepatotoxicants, which are the same as those shown in Fig. 4. Each spot colored by chemical types represents individual samples. Gene expression profiles of rats treated with bromobenzene did not show an apparent shift away from corresponding controls 3 and 6 hr after treatment. Those 9 and 24 hr after treatment showed an apparent shift from the controls.

difference in the content of probe sets, compared with that identified from BSO-treated rats was observed, for instance, glutathione *S*-transferase genes or metallothionein genes, which were induced by BSO but not by phorone (Kiyosawa *et al.*, 2004). Although the strain and the age of the rats were not matched between the two studies (6 week old male Crj:CD(SD)IGS rats vs. 9 week old male F344Cu/Drj rats) the difference could be mainly due to the difference of the GSH-depleting mechanism between phorone and BSO.

To examine the toxicological significance of the GSH probe sets, we conducted PCA on GeneChip data obtained from rats treated with 13 prototypical hepatotoxicants (Fig. 4). On the PCA map, rats treated with bromobenzene, coumarin, and acetaminophen showed apparent changes in hepatic gene expression profiles, and those treated with thioacetamide showed slight changes (Fig. 4). Bromobenzene-treated rats showed the most notable change in gene expression. Bromobenzene was reported to be oxidized to a reactive metabolite in liver, depleting hepatic glutathione (Chakrabarti, 1991; Heijne *et al.*, 2004).

Courmarin-treated rats showed the second most affected gene expression profile in PCA. It was reported that a single coumarin treatment reduced the hepatic content of non-protein sulfhydryl groups (Lake *et al.*, 1989), and this is thought to reflect the decrease in glutathione content. Furthermore, coumarin was shown to decrease glutathione content in rat hepatocyte as well (Lake *et al.*, 1989). Reactive metabolites generated from coumarin oxidation in liver were thought to play a role in coumarin-induced glutathione depletion and hepatotoxicity (Lake, 1984; Lake *et al.*, 1989). Since no apparent hepatotoxicity was evident in both the histopathology and plasma biochemistry data (Table 2), the PCA result would reflect the potential risk of courmarin-induced glutathione-depletion.

Acetaminophen and thioacetamide are known to deplete or reduce glutathione in liver when overdosed (Mesa *et al.*, 1996). In the present study, acetaminophen- or thioacetamide treated rat showed no dramatic change in the gene expression profile compared to bromobenzene. Considering the plasma chemistry data, rats treated with acetaminophen or thioacetamide did not show apparent hepatotoxicity within 24 hr after single dose, whereas those treated with bromobenzene apparently showed it, suggesting that glutathione depletion, expression profile of GSH probe sets, and toxicological phenotype are well correlated with each other.

We also investigated the time-course of glutathione content and gene expression profile in rat livers treated with bromobenzene, and this showed the most notable gene expression change of all of the examined hepatotoxicants (according to the PCA result). Bromobenzene rapidly depleted hepatic glutathione 3 hr after treatment, and the glutathione content was the lowest 9 hr after treatment (Fig. 5). Hepatic glutathione content recovered from initial depletion until 24 hr after the bromobenzene treatment, and such recovery has been previously reported (Chakrabarti, 1991; Heijne *et al.*, 2004). On the other hand, gene expression changes had not been apparent 3 and 6 hr after the bromobenzene treatment, but appeared 9 and 24 hr after treatment. Although hepatic glutathione content was recovered at 24 hr after the bromobenzene treatment, a changed level in gene expression was most prominent at this time point. This result depicts a characteristic of the gene expression profile in that it does not reflect the status of hepatic glutathione content itself, but the nuclear activity to maintain glutathione homeostasis in the liver against bromobenzene-induced glutathione depletion. It should be noted, that although the hepatic glutathione content was recovered 24 hr after bromobenzene treatment, the potential risk of bromobenzene-induced glutathione depletion does exist. In general, hepatic glutathione depletion caused by chemical treatments occurs immediately, followed by rapid recovery by glutathione re-synthesis (Meister and Anderson, 1983). Since the time point of sacrifice in ordinal toxicity studies is set to 24 hr after chemical treatment in many cases, measurement of glutathione content might overlook the risk of the glutathione-depleting potential of the tested chemicals, because 24 hr is enough time for the recovery of glutathione content after acute glutathione depletion. Instead, gene expression profiling is considered to be appropriate for evaluating the glutathione-depleting potential of chemicals, rather than measuring glutathione content, especially in later time points of chemical treatment. This characteristic of gene expression profiling, namely toxicogenomics analysis, would allow for safety assessment of chemicals in drug development.

In conclusion, a total of 161 probe sets of RAE 230A GeneChip, referred as GSH probe sets, were identified using phorone-treated rats for evaluation of drug-induced glutathione depletion. The significance of the identified GSH probe sets was evaluated using the TGP database, where prototypical glutathione depletors successfully showed characteristic changes in the signal levels of GSH probe sets. The time-course

of glutathione content and the gene expression profile showed that gene expression profiling could detect the glutathione-depleting potential of chemicals in later time points, e.g., 24 hr after chemical treatment, where hepatic glutathione content had recovered from acute and transient depletion at earlier time points. Therefore, toxicogenomics analysis using identified GSH probe sets would be an invaluable methodology for assessing a drug's potential risk of glutathione depletion, possibly leading to hepatotoxicity.

ACKNOWLEDGMENT

This study was supported in part by a grant from the Ministry of Health, Labor and Welfare (H14-Tox-ico-001).

REFERENCES

Boverhof, D.R. and Zacharewski, T.R. (2006) : Toxicogenomics in risk assessment: Applications and needs. Toxicol. Sci., **89**, 352-360.

Boyland, E. and Chasseaud, L.F. (1967) : Enzyme-catalysed conjugations of glutathione with unsaturated compounds. Biochem. J., **104**, 95-102.

Chakrabarti, S.(1991): Potential tolerance against bromobenzene-induced acute hepatotoxicity due to prior subchronic exposure. Arch. Toxicol., **65**, 681-684.

Dahlin, D.C., Miwa, G.T., Lu, A.Y. and Nelson, S.D. (1984): *N*-acetyl-*p*-benzoquinone imine: a cytochrome P-450-mediated oxidation product of acetaminophen. Proc. Natl. Acad. Sci. U S A, **81**, 1327-1231.

Heijne, W.H., Slitt, A.L., Van Bladeren, P.J., Groten, J.P., Klaassen, C.D., Stierum, R.H. and Van Ommen, B. (2004): Bromobenzene-Induced Hepatotoxicity at the Transcriptome Level. Toxicol. Sci., **79**, 411-422.

James, L.P., Mayeux, P.R. and Hinson, J.A. (2003): Acetaminophen-induced hepatotoxicity. Drug. Metab. Dispos., **31**, 1499-1506.

Kaplowitz, N.(2004): Drug-induced liver injury. Clin. Infect. Dis., **38**, Suppl. 2, S44-48.

Kiyosawa, N., Ito, K., Sakuma, K., Niino, N., Kanbori, M., Yamoto, T., Manabe, S. and Matsunuma, N. (2004): Evaluation of glutathione deficiency in rat livers by microarray analysis. Biochem. Pharmacol., **68**, 1465-1475.

Lake, B.G. (1984): Investigations into the mechanism of coumarin-induced hepatotoxicity in the rat. Arch. Toxicol., Suppl. **7**, 16-29.

Lake, B.G., Gray, T.J., Evans, J.G., Lewis, D.F., Beamand, J.A. and Hue, K.L. (1989): Studies on the mechanism of coumarin-induced toxicity in rat hepatocytes: Comparison with dihydrocoumarin and other coumarin metabolites. Toxicol. Appl. Pharmacol., **97**, 311-323.

Li, A.P. (2002): A review of the common properties of drugs with idiosyncratic hepatotoxicity and the "multiple determinant hypothesis" for the manifestation of idiosyncratic drug toxicity. Chem. Biol. Interact., **142**, 7-23.

Liu, G., Loraine, A.E., Shigeta, R., Cline, M., Cheng, J., Valmeekam, V., Sun, S., Kulp, D. and Siani-Rose, M.A. (2003): NetAffx: Affymetrix probesets and annotations. Nucleic Acids Res., **31**, 82-86.

Lu, S.C. (1999): Regulation of hepatic glutathione synthesis: Current concepts and controversies. Faseb J., **13**, 1169-1183.

Meister, A. and Anderson, M.E. (1983) Glutathione. Ann. Rev. Biochem., **52**, 711-760.

Mesa, M.L., Carrizosa, R., Martinez-Honduvilla, C., Benito, M. and Fabregat, I. (1996): Changes in rat liver gene expression induced by thioacetamide: Protective role of S-adenosyl-L-methionine by a glutathione-dependent mechanism. Hepatology, **23**, 600-606.

Mitchell, J.R., Jollow, D.J., Potter, W.Z., Gillette, J.R. and Brodie, B.B. (1973): Acetaminophen-induced hepatic necrosis. IV. Protective role of glutathione. J. Pharmacol. Exp. Ther., **187**, 211-217.

Moinova, H.R. and Mulcahy, R.T. (1999): Up-regulation of the human gamma-glutamylcysteine synthetase regulatory subunit gene involves binding of Nrf-2 to an electrophile responsive element. Biochem. Biophys. Res. Commun., **261**, 661-668.

Nguyen, T., Sherratt, P.J. and Pickett, C.B. (2003): Regulatory mechanisms controlling gene expression mediated by the antioxidant response element. Ann. Rev. Pharmacol. Toxicol., **43**, 233-260.

Orphanides, G.(2003): Toxicogenomics: Challenges and opportunities. Toxicol. Lett., **140-141**, 145-148.

Parkinson, A. (2001): Biotransformation of xenobiotics. In (Klaassen, C.D., ed.), pp. 133-224, Casarett and Doull's Toxicology, McGraw-Hill,

New York.

Rockett, J.C. and Dix, D.J. (2000): DNA arrays: Technology, options and toxicological applications. Xenobiotica, **30**, 155-177.

Snedecor, G.W. and Cochran, W.G. (1989): Statistical Methods, 8th ed., Iowa State University Press.

Takashima, K., Mizukawa, Y., Morishita, K., Okuyama, M., Kasahara, T., Toritsuka, N., Miyagishima, T., Nagao, T. and Urushidani, T. (2006): Effect of the difference in vehicles on gene expression in the rat liver-analysis of the control data in the Toxicogenomics Project Database. Life Sci., **78**, 2787-2796.

Urushidani, T. and Nagao, T. (2005): Toxicogenomics: the Japanese initiative. In (Borlak, J., ed.), pp. 623-631, Handbook of Toxicogenomics-Strategies and Applications Wiley-VCH.

van Doorn, R., Leijdekkers, C.M. and Henderson, P.T.(1978): Synergistic effects of phorone on the hepatotoxicity of bromobenzene and paracetamol in mice. Toxicology, **11**, 225-233.

Available online at www.sciencedirect.com
ScienceDirect
Biomaterials 28 (2007) 2612–2621
Biomaterials
www.elsevier.com/locate/biomaterials

The effect of the microstructure of β-tricalcium phosphate on the metabolism of subsequently formed bone tissue

Takatoshi Okuda[a,b], Koji Ioku[c], Ikuho Yonezawa[b], Hideyuki Minagi[d], Giichiro Kawachi[c,1], Yoshinori Gonda[a,b], Hisashi Murayama[e], Yasuaki Shibata[a], Soichiro Minami[f], Shimeru Kamihira[g], Hisashi Kurosawa[b], Tohru Ikeda[a,*]

[a]*Department of Oral Pathology and Bone Metabolism, Unit of Basic Medical Sciences, Nagasaki University Graduate School of Biomedical Sciences, 1-7-1 Sakamoto, Nagasaki 852-8588, Japan*
[b]*Department of Orthopedic Surgery, School of Medicine, Juntendo University, 2-1-1 Hongo, Bunkyo-ku, Tokyo 113-8421, Japan*
[c]*Graduate School of Environmental Studies, Tohoku University, 6-6-20 Aoba, Sendai, Miyagi 980-8579, Japan*
[d]*Technical Research Laboratory, Toyo Kohan Co. Ltd., Kudamatsu, Yamaguchi 744-8611, Japan*
[e]*Kureha Special Laboratory Co. Ltd., 3-26-2 Hyakunin-cho, Shinjuku-ku, Tokyo 169-8503, Japan*
[f]*Division of Laboratory Medicine, Nagasaki University Hospital of Medicine and Dentistry, 1-7-1 Sakamoto, Nagasaki 852-8501, Japan*
[g]*Department of Laboratory Medicine, Unit of Translational Medicine, Nagasaki University Graduate School of Biomedical Sciences, 1-12-4 Sakamoto, Nagasaki 852-8523, Japan*

Received 21 November 2006; accepted 31 January 2007
Available online 20 February 2007

Abstract

The response of bone cells to a newly developed porous β-tricalcium phosphate composed of rod-shaped particles (RSβ-TCP), β-TCP composed of conventional non-rod-shaped particles (Cβ-TCP), and hydroxyapatite (HA) was analyzed using in vivo implantation and in vitro osteoclastogenesis systems. Implantation of the materials into the rabbit femur showed that RSβ-TCP and Cβ-TCP were bioresorbable, but HA was not. Up to 12 weeks after the implantation, bioresorption of RSβ-TCP and Cβ-TCP accompanied by the formation of new bone occurred satisfactorily. At 24 weeks post-implantation, most of the RSβ-TCP had been absorbed, and active osteogenesis was preserved in the region. However, in the specimens implanted with Cβ-TCP, the amount of not only the implanted Cβ-TCP but also the newly formed bone tissue decreased, and bone marrow dominated the region. The implanted HA was unbioresorbable throughout the experimental period. When osteoclasts were generated on RSβ-TCP, Cβ-TCP, or HA disks, apparent resorption lacunae were formed on the RSβ-TCP and Cβ-TCP, but not HA disks. Quantitation of the calcium concentration in the culture media showed an earlier and more constant release of calcium from RSβ-TCP than Cβ-TCP. These results showed that the microstructure of β-TCP affects the activity of bone cells and subsequent bone replacement.

Keywords: Biodegradation; Bone graft; Coculture; Osteoblast; Osteoclast

1. Introduction

In place of bone autografts and allografts, implantations of bone substitutes have been tried experimentally or performed clinically. The major advantages of using bone substitutes are the prevention of additional surgery to take autograft bone, prevention of the transfer of disease from an allograft, and prevention of immunological reactions to the allograft. In addition, bone substitutes can be very useful in patients who cannot provide a sufficient amount of bone tissue for an autograft or patients who cannot provide healthy bone tissue because of osteoporosis. The major inorganic component of bone tissue is hydroxyapatite (HA), and many different calcium phosphate ceramics have been utilized as a material for bone substitutes [1]. As

*Corresponding author. Tel.: +81 95 849 7644; fax: +81 95 849 7644.
E-mail address: tohrupth@net.nagasaki-u.ac.jp (T. Ikeda).
[1]Present address: Department of Crystalline Materials Science, Graduate School of Engineering, Nagoya University, Furo-cyo, Chikusa-ku, Nagoya 464-8603, Japan.

0142-9612/$ - see front matter © 2007 Elsevier Ltd. All rights reserved.
doi:10.1016/j.biomaterials.2007.01.040

a bone substitute, HA is highly osteocompatible and expresses sufficient osteoconductivity, but stoichiometric HA is unbioresorbable, and has much less mechanical strength than bone tissue because there is no organic component such as type I collagen in the bone substitute. Therefore, the HA that remains in bone tissue can cause serious clinical problems.

Bioresorbable bone substitutes have also been developed to prevent the implant from remaining in the bone tissue. Beta-tricalcium phosphate (β-TCP) is one of the most popular bioresorbable materials for bone substitutes. However, the osteogenic activity of β-TCP is thought to be poor and the application of this material tends to be restricted to relatively small bone defects [2,3]. The osteoinduction of β-TCP has been improved using bone morphogenetic protein-2 (BMP-2) [3–7]. However, the high cost of using a large amount of BMP prevents widespread use of this method. Tissue engineering is another fascinating way to improve the prognosis of the grafted β-TCP. Adding osteoprogenitor cells on the graft material has also been reported to improve replacement of the bone substitute by newly formed bone tissue [8–10]. However, the culture of osteoprogenitor cells on bone substitutes before implantation requires great care to prevent infections, and additional efforts are needed to spread this technique in the clinical field. Some inconsistency in the prognosis after the implantation of β-TCP has also been reported. In some cases, the implanted β-TCP remained in the bone tissue, whereas in others, it dissolved almost completely, and the extent of the subsequent bone replacement varied [11–14]. The difference might depend on the activities of bone cells in the recipients, but there is as yet no biological explanation for this discrepancy. All this would suggest that the development of new materials suitable for bone substitutes is still very important, and may lead to great improvements in this field.

Ioku et al. established a hydrothermal method to synthesize HA, and developed an unique fibrous apatite [15]. The hydrothermal approach has several advantages over the sintering method; it does not need expensive equipment, the cost of production is relatively low, and the method can be used to synthesize many kinds of ceramic particles. Then, we applied the hydrothermal method to the synthesis of β-TCP, and succeeded in developing an unique porous β-TCP composed of rod-shaped particles (RSβ-TCP) [16]. The particles are about 10–20 μm in length, and tangled together form micro-pores about 0.1–0.5 μm in size. We previously reported that micro-pores 0.2–0.5 μm in size were effective at improving the bioresorption of β-TCP in bone [17], and RSβ-TCP was expected to be an appropriate material for bone substitutes. Recently, we implanted RSβ-TCP in the rabbit femur, and showed that the material exhibited good osteoconductivity [18].

In the present study, to evaluate the performance of RSβ-TCP as a bone substitute more precisely, we compared biodegradability and bone replacement after the implantation of RSβ-TCP to those after the implantation of conventional β-TCP composed of non-rod-shaped particles (Cβ-TCP) or HA using the rabbit implantation system. In addition, we quantitatively analyzed the bioresorption of these materials using a newly developed in vitro evaluation system. These experiments revealed considerable differences between RSβ-TCP and Cβ-TCP.

2. Materials and methods

2.1. Preparation of implants

Cylindrical implants of RSβ-TCP 6 mm in diameter and 10 mm in length were prepared using an applied hydrothermal method described previously [18]. The powder of α-tricalcium phosphate was formed into cylindrical shape by uniaxial compressing. The formed sample was set in a 105 cm^3 autoclave with 10 cm^3 of dilute aqueous ammonia and exposed to vapor of the solution at 160 °C under a saturated vapor pressure for 20 h, and then heated at 900 °C for 3 h in air. Cβ-TCP implants of the same shape and size were prepared from the powder of β-TCP by normal sintering at 900 °C in air. HA implants of the same shape and size were prepared from a powder of stoichiometric HA with a Ca/P molar ratio of 1.67 by normal sintering at 1200 °C in air as reported previously. For each implant, holes 350 μm in diameter were created vertically and horizontally.

2.2. Animals and operative procedures

Forty-eight female Japanese White rabbits, 3 months of age with a body weight ranging from 2.3 to 2.4 kg, were used for this study. Rearing of these animals and animal experiments were performed at the Biomedical Research Center, Center for Frontier Life Sciences, Nagasaki University, following the Guidelines for Animal Experimentation of Nagasaki University (Approval No. 0502020400). The rabbits were anesthetized with an intramuscular injection of ketamine (60 mg/kg body weight) and xylazine (3 mg/kg body weight) before surgery. To prevent infection, a subcutaneous injection of orbifloxacin (3 mg/kg body weight) was used just before surgery. Under sterile conditions, the distal metaphysis and lateral condyle of the left femur were exposed through a 3-cm long lateral longitudinal skin incision and the thigh muscles were divided. A dead-end defect, 6 mm in diameter and 10 mm in depth, was created in the lateral cortex just proximal to the epiphyseal plate using a surgical drill. The orientation of the defect was perpendicular to the sagittal axis of the femur. The hole was irrigated with saline (0.9%), each test implant was carefully inserted into the hole manually, and the wound was closed layer by layer. Four rabbits were used for each of the RSβ-TCP, Cβ-TCP, and HA implants. The experimental animals were sacrificed by means of an overdose of anesthetic 2, 4, 12, and 24 weeks after the operation. For fluorescent labeling of the bone tissue, calcein (Wako Pure Chemical Industries, Osaka, Japan) was subcutaneously injected (20 mg/kg body weight) 7 days and 1 day before sacrifice at 2 weeks after the operation, 7 days and 2 days before sacrifice at 4 weeks after the operation, and 10 days and 3 days before sacrifice at 12 weeks and 24 weeks after the operation.

2.3. Radiological and histological analyses

The distal portion of the left femur was dissected from the sacrificed animals, and X-ray photographs were taken using a soft X-ray apparatus (TRS-1005, SOFRON, Tokyo, Japan). All the harvested tissue specimens were fixed in 4% formaldehyde in 0.1 M phosphate buffer (pH 7.2), embedded in 2-hydroxyethyl methacrylate/methyl methacrylate/2-hydroxyethyl acrylate mixed resin, and sectioned 3 μm thick. These sections were stained with toluidine blue or histochemically stained for tartrate-resistant acid phosphatase (TRAP) activity as described previously [19]. The adherent sectioning was performed using Cryofilm Type I (Finetec, Tokyo, Japan). The 3-μm thick sections were made after the adhesion of

the film on the cut surface of the plastic-embedded block. These sections were stained for TRAP activity.

2.4. Histomorphometry

Histomorphometric analyses were performed using the Osteoplan II system (Carl Zeiss, Thornwood, NY) as described previously [20]. Bone volume/tissue volume (BV/TV, %), bone formation rate/bone surface (BFR/BS, $mcm^3/mcm^2/d$), mineral apposition rate (MAR, mcm/d), number of osteoclasts/bone perimeter (N.Oc/B.Pm, per 100 mm), and osteoclast surface/bone surface (Oc.S/BS, %) were calculated for each sample in 3 squares with sides 1.2 mm long, which were arranged in a square field inscribed in a circle 6 mm in diameter. The 3 squares were arranged in two distal corners and the center of the inscribed square. An osteoclast was defined as a multinucleated cell in contact with the surface of a bone or bone substitute. MAR was calculated under a fluorescence microscope at a wavelength of 455 nm. To calculate BV/TV, N.Oc/B.Pm, Oc.S/BS, and BFR/BS, sections stained with toluidine blue were used. Statistical differences were evaluated using the t-test.

2.5. In vitro experiments

Osteoclasts were generated as described previously [21]. Briefly, mouse bone marrow macrophages prepared from the femora and tibiae of 5-week-old female ddY mice were expanded in vitro in a culture medium composed of α-minimal essential medium supplemented with 10% fetal bovine serum and 30 ng/ml of macrophage colony-stimulating factor (Sigma, St. Louis, MO). Then, the macrophages (2×10^4 cells/well) were mixed with NIH3T3 cells expressing human RANKL cDNA [21] (2×10^4 cells/well) and seeded in 24-well plates in which one RSβ-TCP, Cβ-TCP, or HA disk 10 mm in diameter was inserted per well. All the ceramic disks were presoaked in α-minimal essential medium supplemented with 10% fetal bovine serum for a week before being used for the experiments. The soaking medium was changed twice a week. The medium of the cocultures was changed every 3 days up to day 12 of the culture period, and the conditioned medium of each sample was stored at 4 °C. The calcium concentration in each of the conditioned media was analyzed using a JCA-BM12 automatic analyzer (JEOL, Tokyo, Japan) and Diacolor Liquid Ca Kit (Toyobo, Osaka, Japan). The mean concentration of 8 wells for each experimental group was calculated. Statistical differences were evaluated using the Turkey–Kramer method.

The disks used for the experiment were fixed with 4% formaldehyde in 0.1 M phosphate buffer (pH 7.2) and stained for TRAP activity. Resorption lacunae were viewed using a VH-7000 digital microscope (KEYENCE, Osaka, Japan).

3. Results

3.1. General features of samples

The synthesized RSβ-TCP and Cβ-TCP were analyzed by powder X-ray diffractometry with graphite-monochromatized CuKα radiation, operating at 40 kV and 20 mA (XRD; Multi Flex, Rigaku, Tokyo, Japan). No phase other than β-TCP was detected for RSβ-TCP and Cβ-TCP (refer to JCPDS file # 9-169) (Fig. 1). From these results, both RSβ-TCP and Cβ-TCP were considered to be synthesized appropriately. The surface of RSβ-TCP and Cβ-TCP was analyzed by scanning electron microscope (JSM-T300, JEOL, Tokyo, Japan). RSβ-TCP was composed of rod-shaped particles about 20 μm in length, which were tangled together to form micropores about 0.2 μm in size (Fig. 2a). Cβ-TCP was composed of globular particles, which fused

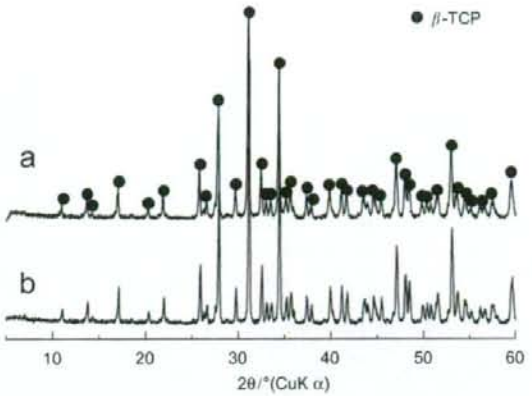

Fig. 1. X-ray diffractometry (XRD) of the implant materials used in this study. XRD patterns of the RSβ-TCP ceramic (a) and Cβ-TCP ceramic (b).

to one another and formed micro-pores about 0.5 μm in size (Fig. 2b). The HA prepared by normal sintering was also analyzed with XRD and no phases other than HA were revealed (data not shown). There is no decomposition as a result of sintering because the HA was stoichiometric. The porosity of RSβ-TCP, Cβ-TCP, and HA was 70% and the mean compressive strength was 8, 2, and 2 MPa, respectively.

3.2. Radiological and histological analyses

Fig. 3 represents radiographs of rabbit femurs 4, 12, and 24 weeks after the operation. At 4 weeks post-surgery, the implanted RSβ-TCP was recognized clearly by its amorphous radiopacity on the X-ray photograph (Fig. 3a). At 12 weeks, radiopacity derived from RSβ-TCP was still evident, but the margin was unclear and the area was smaller than that of the specimen 4 weeks after the operation (Fig. 3b). At 24 weeks post-surgery, the amorphous radiopacity of the implanted RSβ-TCP was replaced almost completely by radiopacity derived from a trabecular structure. In addition, higher radiopacity of the area than the surrounding bone tissue was evident (Fig. 3c). In radiographic appearance, the implanted Cβ-TCP was almost identical to RSβ-TCP at 4 and 12 weeks post-surgery (Figs. 3d, e). Twenty-four weeks after the operation, the area of the Cβ-TCP implant was obscure, and the higher radiopacity found in the specimen 24 weeks after the implantation of RSβ-TCP was no longer evident (Fig. 3f). The radiopacity derived from HA was almost unchanged from 4 weeks to 24 weeks after the operation (Figs. 3g–i).

Histological analyses were conducted using the plastic-embedded undecalcified sections stained with toluidine blue or sections stained for TRAP activity. Two weeks after the implantation of RSβ-TCP, many TRAP-positive osteoclasts were seen on the surface of the implant, the edges had a ragged appearance, and there was direct

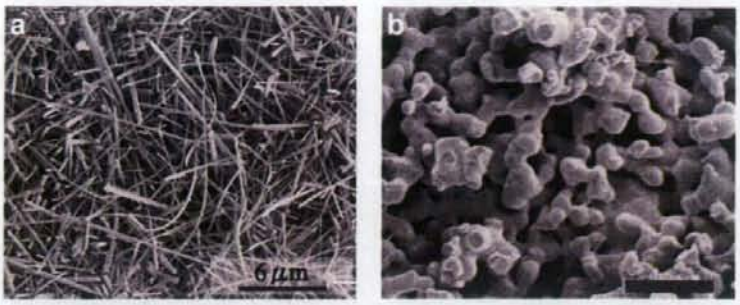

Fig. 2. Scanning electron micrographs of the microstructure of RSβ-TCP (a) and Cβ-TCP (b).

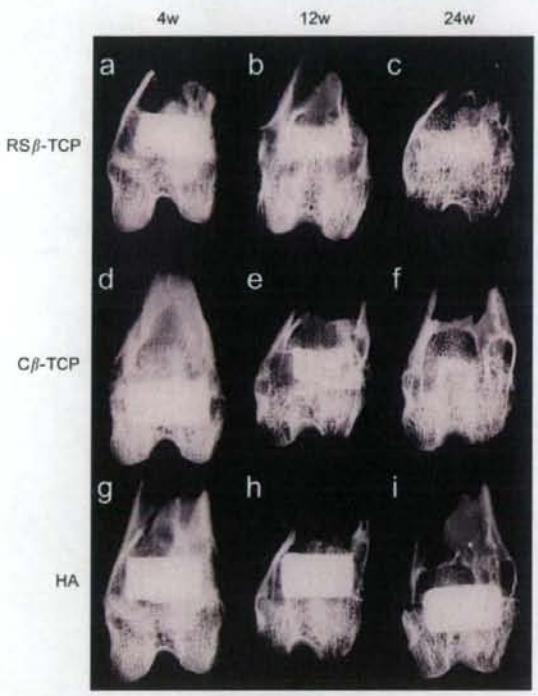

Fig. 3. Soft X-ray photographs of the operated portion of the rabbit femur. Four weeks (a), 12 weeks (b), and 24 weeks (c) after implantation of RSβ-TCP, 4 weeks (d), 12 weeks (e), and 24 weeks (f) after implantation of Cβ-TCP, and 4 weeks (g), 12 weeks (h), and 24 weeks (i) after implantation of HA. Involvement of the implant in bone tissue was evident in the specimen implanted with RSβ-TCP at 12 weeks (b) and 24 weeks (c). In the specimen implanted with Cβ-TCP, involvement of the implant in bone tissue was evident at 12 weeks (e), but not at 24 weeks (f).

contact between the implant and bone (Fig. 4a). Four weeks after the implantation of RSβ-TCP, the invasion of not only TRAP-positive osteoclasts, but also newly formed bone, into the implant was evident (Fig. 4b, arrows). However, much of the implant material remained (Fig. 4b, *). Twelve weeks after the operation, the bioresorption of RSβ-TCP and replacement by newly formed bone tissue were greatly increased compared with the findings at 4 weeks post-surgery (Figs. 4b, c). Infiltration by TRAP-positive osteoclasts was also evident (Fig. 4c). Twenty-four weeks after the operation, a small amount of RSβ-TCP still remained. However, the amount of newly formed bone was increased compared with that at 12 weeks (Figs. 4c, d). Infiltration by TRAP-positive osteoclasts was still evident (Fig. 4d).

In the specimens implanted with Cβ-TCP, infiltration by TRAP-positive osteoclasts, bioresorption of the implants, and the formation of new bone tissue were enhanced as in the specimens implanted with RSβ-TCP until 12 weeks after the operation (Figs. 5a–c). Whereas 24 weeks after the operation, the amount of not only the implanted Cβ-TCP, but also the newly formed bone tissue, which was clearly observed 12 weeks after the operation, decreased and fatty bone marrow dominated the region. TRAP-positive osteoclasts were rarely observed in the region (Fig. 5d).

In the specimens implanted with HA, no evidence of bioresorption of the implant was seen throughout the experimental period (Fig. 6). TRAP-positive osteoclasts were seen on the surface of the implant 2 weeks after the operation, and the number decreased as the experiment progressed. On the other hand, bone contact was evident 2 weeks after the operation (Fig. 6a). Newly formed bone tissue was seen only in the holes created in the implants (Fig. 6b). To evaluate the fine structure of the newly formed bone tissue in the specimens 12 weeks after the operation, sections made with the adherent film were analyzed. As shown in Figs. 7a, b, trabeculae in the specimens 12 weeks after the implantation of RSβ-TCP and Cβ-TCP exhibited a mosaic structure composed of the bone substitute and newly formed bone tissue.

3.3. Histomorphometry

Histomorphometric quantitation revealed BV/TV in the specimens implanted with RSβ-TCP was significantly greater than that in the specimens implanted with Cβ-TCP (Fig. 9a). The fluorescent signal derived from calcein

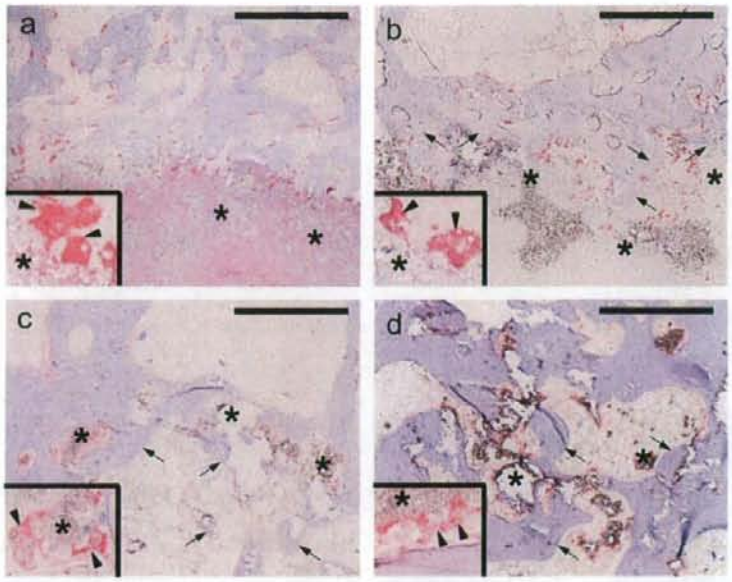

Fig. 4. Histological appearance of a specimen implanted with RSβ-TCP. Two weeks (a), 4 weeks (b), 12 weeks (c), and 24 weeks (d) after the operation. Sections were stained for TRAP activity. Insets show high power view of osteoclasts attached to the bone substitute in each sample (arrowheads). Asterisks (*) represent the implanted bone substitute. Arrows indicate newly formed bone. Bar: a–d, 500 μm.

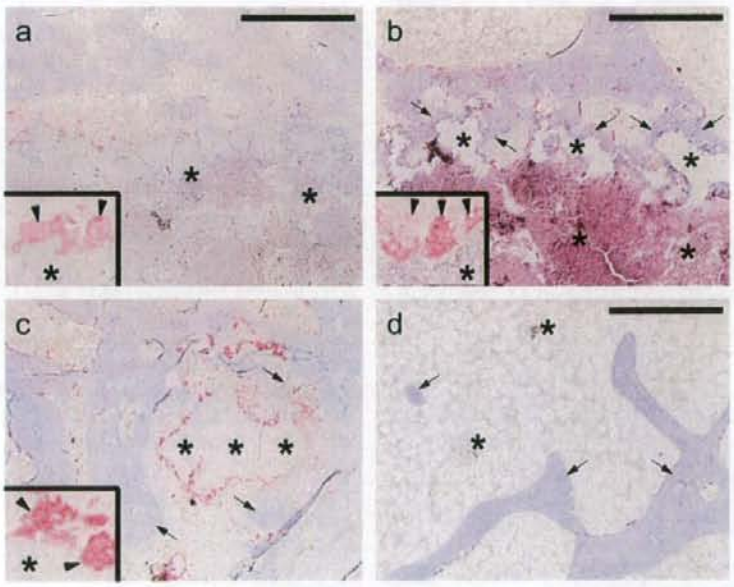

Fig. 5. Histological appearance of a specimen implanted with Cβ-TCP. Two weeks (a), 4 weeks (b), 12 weeks (c), and 24 weeks (d) after the operation. Sections were stained for TRAP activity. Insets show high power view of osteoclasts attached to the bone substitute in each sample (arrowheads). Asterisks (*) represent the implanted bone substitute. Arrows indicate newly formed bone. Bar: a–d, 500 μm.

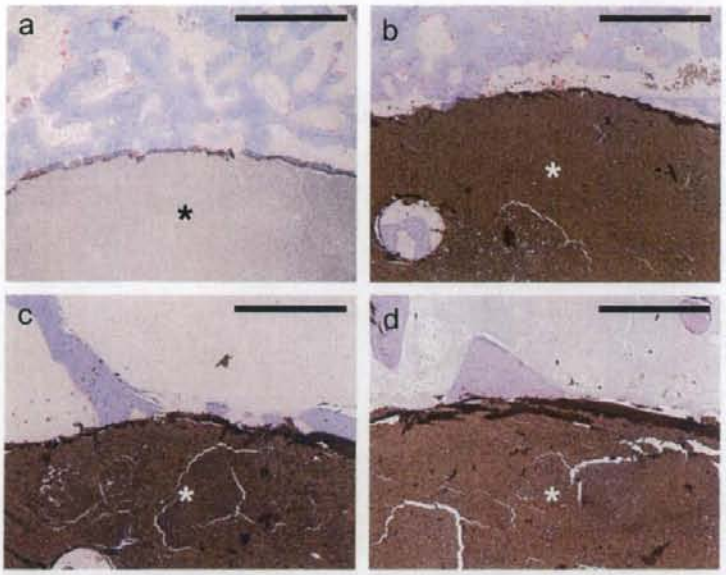

Fig. 6. Histological appearance of a specimen implanted with HA. Two weeks (a), 4 weeks (b), 12 weeks (c), and 24 weeks (d) after the operation. Sections were stained for TRAP activity. Asterisks (*) represent the implanted bone substitute. Bar: a–d, 500 μm.

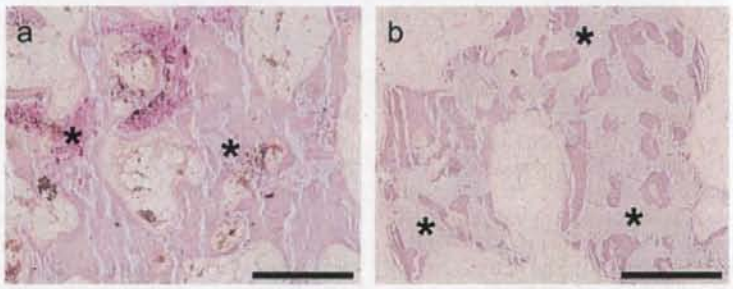

Fig. 7. Fine histological appearance of newly formed bone in specimens made by the method of adherent sectioning. Twelve weeks after the implantation of RSβ-TCP (a) and Cβ-TCP (b). Sections were stained for TRAP activity. Note the mosaic structure of the newly formed bone trabeculae. Asterisks (*) represent the implanted bone substitute. Bar: a, b, 500 μm.

labeling was analyzed using a fluorescence microscope in the specimens 24 weeks after the implantation of either RSβ-TCP or Cβ-TCP. The width of the double labeling, and the amount of bone mass with the signal was much greater in the specimens implanted with RSβ-TCP than those implanted with Cβ-TCP (Fig. 8). Histomorphometric quantitation of BFR/BS and MAR for newly formed bone tissue in each sample is shown in Fig. 9. BFR/BS revealed a strong tendency to increase in the specimens implanted with RSβ-TCP as compared with the specimens implanted with Cβ-TCP (Fig. 9b). MAR was significantly increased in the specimens implanted with RSβ-TCP in comparison to the specimens implanted with Cβ-TCP (Fig. 9c). Additionally, N.Oc/B.Pm and Oc.S/BS were quantified. As shown in Figs. 9d, e, both N.Oc/B.Pm and Oc.S/BS were significantly increased in the specimens implanted with RSβ-TCP compared with those implanted with Cβ-TCP.

3.4. *In vitro analyses of bioresorption by osteoclasts*

To show that the implanted RSβ-TCP and Cβ-TCP were resorbed by osteoclasts, disks made with RSβ-TCP, Cβ-TCP, and HA were used for an in vitro osteoclastogenesis assay. RANKL-expressing fibroblasts and mouse bone marrow macrophages were cocultured on the disks, and the calcium concentration in the culture supernatant was analyzed biochemically. As shown in Fig. 10a, the mean calcium concentration was significantly higher in the culture supernatant of the RSβ-TCP disk than in that of the Cβ-TCP or HA disk at 3 days into the coculture, and

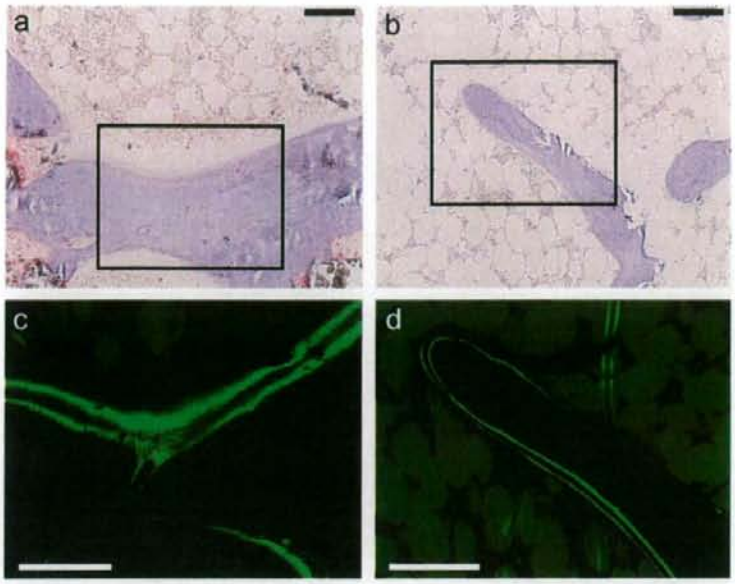

Fig. 8. Evaluation of osteogenesis by fluorescent labeling. (a, b) Bright-field light microscopic appearance of specimens 24 weeks after the implantation of RSβ-TCP (a) and Cβ-TCP (b). Sections were stained for TRAP activity. The squares represent the area used for the fluorescent analysis. (c, d) The calcein signal in the newly formed bone tissue in the specimens 24 weeks after the implantation of RSβ-TCP (c) and Cβ-TCP (d). Sections stained with toluidine blue were utilized for analysis by fluorescence microscopy. Bar: a–d, 100 μm.

gradually increased up to day 12. The calcium concentration in the culture supernatant of cocultures performed on the HA disk was not significantly changed throughout the culture period, and the calcium concentration in the culture supernatant of the RSβ-TCP disk was significantly higher than that of the HA disk on all days analyzed (Fig. 10a). When the coculture was performed on the disk made with Cβ-TCP, the calcium concentration in the culture supernatant was near the basal level on days 3 and 6 of the coculture. Whereas the mean calcium concentration in the culture supernatant of the Cβ-TCP disk increased thereafter and became significantly higher than that of the HA disk at 9 days into the coculture. On day 12 of the coculture, the calcium concentration was significantly higher in the culture supernatant of the Cβ-TCP disk than in that of not only the HA disk, but also the RSβ-TCP disk (Fig. 10a).

Numerous pits, which revealed characteristic features of resorption lacunae formed by osteoclasts, were found on the disks of RSβ-TCP and Cβ-TCP (Figs. 10b, c). On the other hand, no typical resorption lacuna was found on the disks of HA (Fig. 10d). Fig. 10e shows typical features of resorption lacunae formed on a slice of whale dentin.

4. Discussion

Although their application is still restricted, bone substitutes have already been widely used chiefly in the fields of orthopedic surgery and dentistry. One of the most important features of bone substitutes is osteoconductivity, and many kinds of ceramics possessing this feature have been introduced as suitable materials for bone substitutes. In addition to osteoconductivity, biodegradability is another important feature of bone substitutes. Biodegradability should basically be induced by osteoclastic resorption, which accompanies the subsequent formation of new bone.

In the present study, we showed that resorption and replacement with newly formed bone tissue occurred similarly in specimens implanted with either RSβ-TCP or Cβ-TCP up to 12 weeks after the operation. Surprisingly, at 24 weeks after the operation, most of the implant and newly formed bone was absorbed in the specimens implanted with Cβ-TCP, whereas much bone tissue was seen in place of the implanted RSβ-TCP. Few previous papers have stated the course post-implantation of β-TCP in rabbit bones, and a detailed histology of such experiments has not been described. In addition, these experiments were performed using β-TCP differing in porosity to the Cβ-TCP used in the present study [22,23]. Therefore, we could not compare the data on Cβ-TCP to results of previous studies. The data on XRD (Fig. 1) and the views under the scanning electron microscope (Fig. 2) indicated that both RSβ-TCP and Cβ-TCP were highly purified β-TCPs and the difference in the specimens 24 weeks after the implantation was thought to be due to their different microstructures.

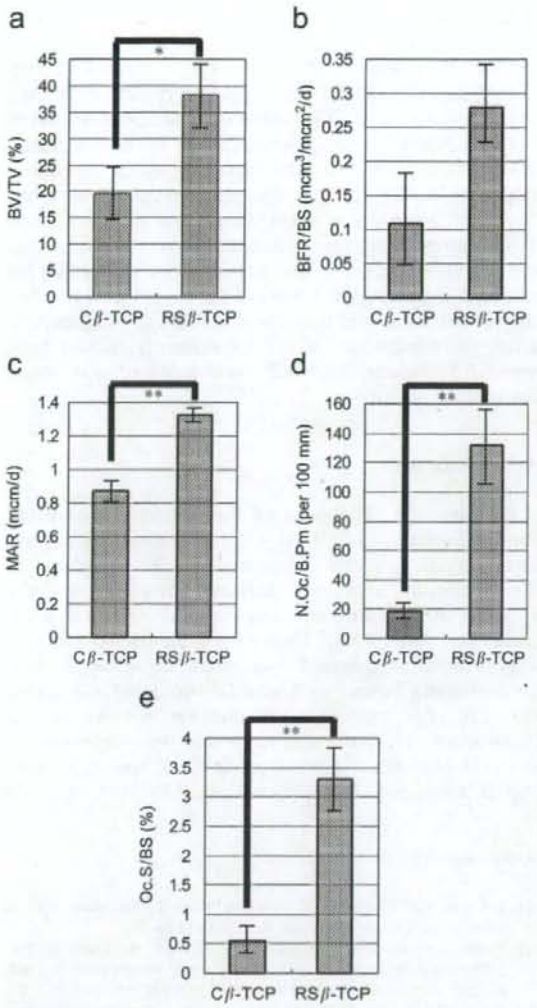

Fig. 9. Histomorphometry of the newly formed bone tissue in the specimens 24 weeks after the implantation. Parameters for the amount of bone, BV/TV (a), osteogenic activity, BFR/BS (b) and MAR (c), were compared between specimens implanted with RSβ-TCP and specimens implanted with Cβ-TCP. Parameters for bone resorption, N.Oc/B.Pm (d) and Oc.S/BS (e), were also compared (*$P<0.05$, **$P<0.01$). Three areas in the four samples were analyzed for the data acquired.

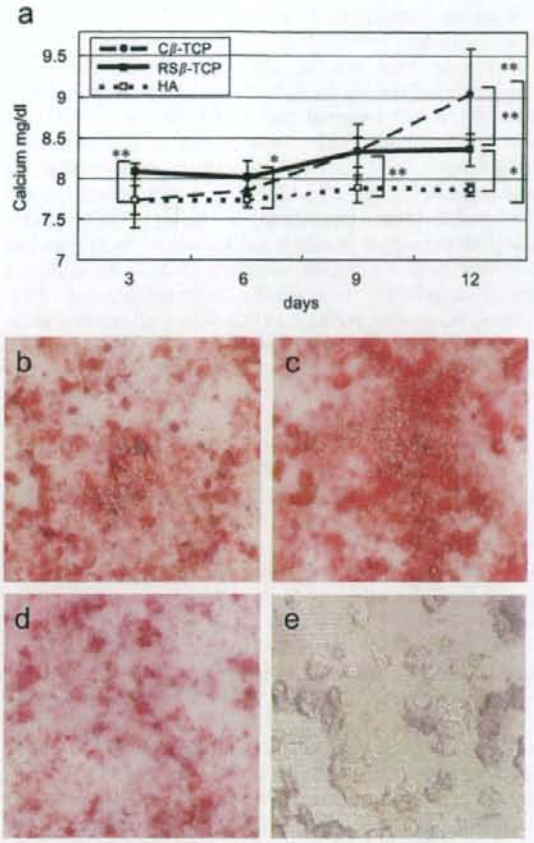

Fig. 10. The in vitro resorption assay of RSβ-TCP, Cβ-TCP, and HA. (a) Change in the calcium concentration of the culture medium in each culture period (*$P<0.05$, **$P<0.01$). (b–d) Enlarged surface structures of RSβ-TCP (b), Cβ-TCP (c), and HA (d) served for the in vitro resorption assay. Disks were stained for TRAP activity. (e) Typical resorption lacunae formed on whale dentin.

Bone metabolism is strictly regulated by a balance of bone resorption and bone formation. Likewise, the metabolism of bone substitutes and newly formed bone would also be strictly regulated by an appropriate balance of resorption and bone formation. Previously, we showed that in the bones of ovariectomized rats, both the number of osteoclasts and the activity of osteoblasts were increased compared with levels in the sham-operated rats before bone volume was significantly decreased [20]. These results strongly suggested that the activation of bone resorption stimulated the formation of bone, but an imbalance of bone resorption and bone formation resulted in bone loss. Many osteoclasts and new bone were seen in the regions where RSβ-TCP and Cβ-TCP were implanted 12 weeks after the operation (Figs. 4c, 5c), and an imbalance of bone metabolism might occur in the animals implanted with Cβ-TCP, which resulted in a loss of newly formed bone and the bone substitute 24 weeks after the operation (Fig. 5d).

The mechanism behind the imbalance is unclear, but we speculate that the excessive bioresorbability of the bone substitute caused a loss of bone tissue formed in place of the bone substitute, and an ideal bone substitute should have proper bioresorbability. Interestingly, intramuscular osteogenesis using β-TCP and BMP-2 often resulted in a loss of ectopically formed bone [24]. This may also occur

due to an imbalance of resorption and bone formation, and insufficient numbers of osteoblast progenitor cells in the muscle may not be able to overtake the active resorption of implanted β-TCP and newly formed bone. Recently, it was reported that β-TCP treated with BMP-2 and bisphosphonate effectively prevented loss of ectopically formed bone tissue in the muscle without affecting osteogenesis [25,26]. In addition, a recent report showed that octacalcium phosphate, a highly biodegradable material, implanted in rabbit femurs was partially resorbed and new bone formation was seen at 2 weeks after the operation, whereas the amount of both implant and newly formed bone was reduced at 12 weeks after the operation [27]. Our in vitro experiments suggested that RSβ-TCP was less bioresorbable than Cβ-TCP, because in the osteoclastogenesis system, multinucleated osteoclasts begin to appear around the 5th day of coculture (data not shown), and the higher calcium concentration in the culture supernatant of Cβ-TCP than that of RSβ-TCP at 9 and 12 days of the coculture was thought to reflect the bioresorbability of these materials. All these results strongly support our hypothesis. However, it is highly possible that "proper bioresorbability" depends on the biological activity of bone cells in the recipient, and varies.

It is also possible that RSβ-TCP possesses the potential to stimulate osteoblastic activity and bone formation. Actually, increased radiopacity and bone mass compared with the surrounding bone tissue were seen in the specimens 24 weeks after the implantation of RSβ-TCP (Fig. 3c, data not shown) in spite of the remarkable fatty change in the bone marrow (Figs. 4d, 8a). Previously, we suggested that micropores of β-TCP affected bone cell activities [17]. The particles composing RSβ-TCP were entangled and formed micropores about 0.2 μm in size (Fig. 2a), and these micropores may effectively adsorb certain kinds of proteins in body fluid and might contribute to the stimulation of osteoblastic activity.

The calcium concentration was significantly increased in the medium cocultured for 3 days on RSβ-TCP compared with Cβ-TCP and HA (Fig. 10a). As described in Section 2, all the disks were presoaked in the culture medium for a week before the coculture, and no significant increase in the calcium concentration was detected in the presoaked medium (data not shown). In addition, although TRAP-positive mononuclear preosteoclasts appeared around the 3rd day of the coculture, multinucleated osteoclasts began to be seen around the 5th day (data not shown). Therefore, the rise in the calcium concentration in the culture supernatant cocultured for 3 days on RSβ-TCP was strongly suggested to be caused by preosteoclastic resorption, and RSβ-TCP may fit with the attachment and/or activation of preosteoclasts. Considering the possibility that it stimulates the activity of osteoblasts, RSβ-TCP may possess unique characteristics and more studies should be done to clarify the influence of microstructure on the biology of bone cells.

5. Conclusion

This study showed that a β-TCP composed of rod-shaped particles (RSβ-TCP) behaved very differently from the conventional β-TCP composed of globular-shaped particles (Cβ-TCP) when implanted in the rabbit femur. Twenty-four weeks after the implantation, the bioresorption of RSβ-TCP and subsequent formation of bone had occurred adequately, whereas the amount of Cβ-TCP and newly formed bone tissue, which was seen at 12 weeks after the operation, decreased and bone marrow dominated the region. Considering the results of the experiments in vitro, the bioresorbability of the bone substitute was suggested to affect the metabolism of the subsequently formed bone tissue. Additionally, RSβ-TCP possibly helped to stimulate osteoblastic activity.

Acknowledgments

We thank Dr. T. Sawase of the Department of Fixed Prosthodontics and Oral Rehabilitation, Nagasaki University for valuable discussions, Dr. K. Hideshima of the Division of Laboratory Medicine, Nagasaki University Hospital of Medicine and Dentistry for technical assistance, and Mr. Ryuji Tsukada of the Department of Experimental Surgery and Biomedical Resources, Juntendo University School of Medicine and Kitayama Labes Co. Ltd. for technical consultations on the animal experiments. This work was supported by a Grant-in-Aid from the Ministry of Education, Culture, Sports, Science, and Technology of Japan (Grant no. 18390519).

References

[1] LeGeros RZ. Properties of osteoconductive biomaterials: calcium phosphates. Clin Orthop Relat Res 2002;395:81–98.
[2] Anker CJ, Holdridge SP, Baird B, Cohen H, Damron TA. Ultraporous beta-tricalcium phosphate is well incorporated in small cavitary defects. Clin Orthop Relat Res 2005;434:251–7.
[3] Komaki H, Tanaka T, Chazono M, Kikuchi T. Repair of segmental bone defects in rabbit tibiae using a complex of beta-tricalcium phosphate, type I collagen, and fibroblast growth factor-2. Biomaterials 2006;29:5118–26.
[4] Matsushita N, Terai H, Okada T, Nozaki K, Inoue H, Miyamoto S, et al. A new bone-inducing biodegradable porous beta-tricalcium phosphate. J Biomed Mater Res A 2004;70:450–8.
[5] Hong SJ, Kim CS, Han DK, Cho IH, Jung UW, Choi SH, et al. The effect of a fibrin-fibronectin/beta-tricalcium phosphate/recombinant human bone morphogenetic protein-2 system on bone formation in rat calvarial defects. Biomaterials 2006;27:3810–6.
[6] Hoshino M, Egi T, Terai H, Namikawa T, Takaoka K. Repair of long intercalated rib defects using porous beta-tricalcium phosphate cylinders containing recombinant human bone morphogenetic protein-2 in dogs. Biomaterials 2006;27:4934–40.
[7] Jung UW, Choi SY, Pang EK, Kim CS, Choi SH, Cho KS. The effect of varying the particle size of beta tricalcium phosphate carrier of recombinant human bone morphogenetic protein-4 on bone formation in rat calvarial defects. J Periodontol 2006;77:765–72.
[8] Boo JS, Yamada Y, Okazaki Y, Hibino Y, Okada K, Hata K, et al. Tissue-engineered bone using mesenchymal stem cells and a

biodegradable scaffold. J Craniofac Surg 2002;13:231–9 [discussion 240–233].
[9] Uemura T, Dong J, Wang Y, Kojima H, Saito T, Iejima D, et al. Transplantation of cultured bone cells using combinations of scaffolds and culture techniques. Biomaterials 2003;24:2277–86.
[10] Wang J, Asou Y, Sekiya I, Sotome S, Orii H, Shinomiya K. Enhancement of tissue engineered bone formation by a low pressure system improving cell seeding and medium perfusion into a porous scaffold. Biomaterials 2006;27:2738–46.
[11] Galois L, Mainard D, Delagoutte JP. Beta-tricalcium phosphate ceramic as a bone substitute in orthopaedic surgery. Int Orthop 2002;26:109–15.
[12] Ogose A, Hotta T, Kawashima H, Kondo N, Gu W, Kamura T, et al. Comparison of hydroxyapatite and beta tricalcium phosphate as bone substitutes after excision of bone tumors. J Biomed Mater Res B Appl Biomater 2005;72:94–101.
[13] Ogose A, Kondo N, Umezu H, Hotta T, Kawashima H, Tokunaga K, et al. Histological assessment in grafts of highly purified beta-tricalcium phosphate (OSferion) in human bones. Biomaterials 2006;27:1542–9.
[14] Zerbo IR, Bronckers AL, de Lange G, Burger EH. Localisation of osteogenic and osteoclastic cells in porous beta-tricalcium phosphate particles used for human maxillary sinus floor elevation. Biomaterials 2005;26:1445–51.
[15] Ioku K, Yamauchi S, Fujimori H, Goto S, Yoshimura M. Hydrothermal preparation of fibrous apatite and apatite sheet. Solid State Ionics 2002;151:147–50.
[16] Ioku K, Minagi H, Yonezawa I, Okuda T, Kurosawa H, Ikeda T, et al. Porous ceramics of β-tricalcium phosphate composed of rod-shaped particles. Arch Bioceram Res 2004;4:121–4.
[17] Yokozeki H, Hayashi T, Nakagawa T, Kurosawa H, Shibuya K, Ioku K. Influence of surface microstructure on the reaction of the active ceramics in vivo. J Mater Sci Mater Med 1998;9:381–4.
[18] Okuda T, Yonezawa I, Ioku K, Minagi H, Kurosawa H, Ikeda T. Porous ceramics of β-tricalcium phosphate composed of rod-shaped particles is highly biodegradable and expresses prominent osteoconductivity. Key Eng Mater 2006;309–311:1063–6.
[19] Ikeda T, Kasai M, Suzuki J, Kuroyama H, Seki S, Utsuyama M, et al. Multimerization of the receptor activator of nuclear factor-kappaB ligand (RANKL) isoforms and regulation of osteoclastogenesis. J Biol Chem 2003;278:47217–22.
[20] Ikeda T, Yamaguchi A, Yokose S, Nagai Y, Yamato H, Nakamura T, et al. Changes in biological activity of bone cells in ovariectomized rats revealed by in situ hybridization. J Bone Miner Res 1996;11:780–8.
[21] Suzuki J, Ikeda T, Kuroyama H, Seki S, Kasai M, Utsuyama M, et al. Regulation of osteoclastogenesis by three human RANKL isoforms expressed in NIH3T3 cells. Biochem Biophys Res Commun 2004;314:1021–7.
[22] Le Huec JC, Clement D, Brouillaud B, Barthe N, Dupuy B, Foliguet B, et al. Evolution of the local calcium content around irradiated beta-tricalcium phosphate ceramic implants: in vivo study in the rabbit. Biomaterials 1998;19:733–8.
[23] Lu JX, Flautre B, Anselme K, Hardouin P, Gallur A, Descamps M, et al. Role of interconnections in porous bioceramics on bone recolonization in vitro and in vivo. J Mater Sci Mater Med 1999;10:111–20.
[24] Jingushi S, Urabe K, Okazaki K, Hirata G, Sakai A, Ikenoue T, et al. Intramuscular bone induction by human recombinant bone morphogenetic protein-2 with beta-tricalcium phosphate as a carrier: in vivo bone banking for muscle-pedicle autograft. J Orthop Sci 2002;7:490–4.
[25] Chen WJ, Jingushi S, Hirata G, Matsumoto Y, Iwamoto Y. Intramuscular bone induction by the simultaneous administration of recombinant human bone morphogenetic protein 2 and bisphosphonate for autobone graft. Tissue Eng 2004;10:1652–61.
[26] Chen WJ, Jingushi S, Jingushi K, Iwamoto Y. In vivo banking for vascularized autograft bone by intramuscular inoculation of recombinant human bone morphogenetic protein-2 and beta-tricalcium phosphate. J Orthop Sci 2006;11:283–8.
[27] Imaizumi H, Sakurai M, Kashimoto O, Kikawa T, Suzuki O. Comparative study on osteoconductivity by synthetic octacalcium phosphate and sintered hydroxyapatite in rabbit bone marrow. Calcif Tissue Int 2006;78:45–54.

Available online at www.sciencedirect.com
ScienceDirect
Biomaterials 28 (2007) 3469–3477
Biomaterials
www.elsevier.com/locate/biomaterials

Enhanced osseointegration by the chemotactic activity of plasma fibronectin for cellular fibronectin positive cells

Ryo Jimbo[a,1], Takashi Sawase[a,1], Yasuaki Shibata[b,*], Kazunari Hirata[c], Yoshitaka Hishikawa[d], Yasuhiro Tanaka[e], Kazuhisa Bessho[f], Tohru Ikeda[b], Mitsuru Atsuta[a]

[a]*Division of Applied Prosthodontics, Nagasaki University Graduate School of Biomedical Sciences, Nagasaki, Japan*
[b]*Division of Oral Pathology and Bone Metabolism, Nagasaki University Graduate School of Biomedical Sciences, Nagasaki, Japan*
[c]*Division of Oral and Maxillofacial Surgery, Nagasaki University Graduate School of Biomedical Sciences, Nagasaki, Japan*
[d]*Division of Histology and Cell Biology, Nagasaki University Graduate School of Biomedical Sciences, Nagasaki, Japan*
[e]*Department of Advanced Materials Science, Faculty of Engineering, Kagawa University, Kagawa, Japan*
[f]*Department of Oral and Maxillofacial Surgery, Graduate School of Medicine, Kyoto University, Kyoto, Japan*

Received 10 January 2007; accepted 13 April 2007
Available online 3 May 2007

Abstract

Plasma fibronectin (pFN) is known to regulate cell growth, differentiation or survival of osteoblasts *in vitro*. It is also speculated to be important for the early phase of osseointegration, however, its actual *in vivo* behavior is unknown. The objective of this study is to clarify the role of pFN during osseointegration. We developed a titanium ion-plated acrylic implant (Ti-acryl) for thin sectioning without removal of the implant. Either Ti-acryl or pFN-coated Ti-acryl (FN-Ti-acryl) was implanted in the mouse femur. Samples were taken on days 1–7 and on day 14 after the operation, and were decalcified and paraffin embedded. The bone healing process and immunofluorescence localization of pFN and cellular fibronectin (cFN), a marker for fibroblastic cells were examined. Simultaneously, the effect of pFN on chemotaxis, proliferation and differentiation of bone marrow stromal cells (BMSCs) was analyzed *in vitro*. The in vivo results showed that faster direct bone formation was seen for the FN-Ti-acryl group compared to the Ti-acryl group. The *in vitro* results showed that pFN significantly promoted BMSCs chemotaxis, however, had no effect on proliferation or differentiation. The results indicate that pFN regulated chemotaxis of osteogenic cells and coating the implant with pFN enhanced earlier osseointegration.

Keywords: Implant; Fibronectin; Osseointegration; Histomorphometry; Chemotaxis

1. Introduction

The faster acquisition of the direct bone to implant anchorage, or so-called osseointegration, is the key factor in the faster functional loading of the implant. Comprehensive efforts and strategies have enhanced osseointegration for increased implant stability [1,2]. For example, the modification of the physical characteristics of the implant by sandblasting or chemical treatment of the implant surface has remarkably improved osseointegration as compared to turned surfaces [3–5]. The reason for such improvement is speculated to be the enhanced adsorption of native blood proteins, such as plasma fibronectin (pFN), onto the implant surface, which enhanced the formation of focal adhesions by osteoblasts through integrin-mediated mechanisms [6,7].

pFN is a prominent extracellular matrix protein [8], which accumulates in the matrix during the early phase of cell growth and attachment [9]. Cellular FN (cFN), an another type of FN, is an insoluble form generated as a result of alternative splicing from a single gene [10]. It is expressed locally by certain fibroblastic cells and other cell types, and is deposited and assembled into the extracellular matrix [11]. It has been suggested that pFN activates the signaling pathways, which direct cell-cycle progression, gene expression and matrix mineralization [12], and even

*Corresponding author. Tel.: +81 95 849 7646; fax: +81 95 849 7647.
E-mail address: siva@nagasaki-u.ac.jp (Y. Shibata).
[1]Equally contributed to the experimental work.

0142-9612/$ - see front matter © 2007 Elsevier Ltd. All rights reserved.
doi:10.1016/j.biomaterials.2007.04.029

regulating the survival of osteoblasts [13]. In fact, coating biomaterial surfaces with pFN *in vitro* has been shown to enhance the formation of focal adhesions by osteoblasts [14] and lead to better cell spreading and cytoskeleton organization compared to non-coated surfaces [15–17]. In addition, it has been reported that pFN adsorbed onto the implant surface when the implant was inserted in the abdominal walls of rats [18]. This evidence suggests that the pFN adsorbed onto the implant surface regulates cellular adhesion and consequent osseointegration. Park et al. [19] have reported that early blood cell/implant interactions which lead to plasma protein accumulation may play a key role in the osteoconduction stage of osseointegration. Rupp et al. [20] have discussed the possible FN adsorption onto endosseous implants via the patient's blood during surgery. However, these reports were only speculations, and the actual behavior of FN at the molecular level *in vivo* around implants during the process of osseointegration remains uncertain. One of the reasons for this is the difficulty in making thin sections without the removal of the implant incorporated into the surrounding bone. Hence, most of the past studies were performed on undecalcified ground sections. Nevertheless, the ground sections clarified the osteoconductive bone regeneration process around the implants histologically and histomorphometrically [21,22], they did not allow for analysis at the molecular level.

We developed an implant coated with a thin film of titanium by means of the ion-plating method [23]. With this implant, the preparation of paraffin-embedded or frozen sections for immunohistochemistry or *in situ* hybridization (ISH) is possible without removing the titanium implant. In this study, by using this implant, the effects of pFN on the osseointegration process in the mice femur histologically and histomorphometrically was examined, followed by immunofluorescence observation with pFN antibody and cFN antibody. Simultaneously, the effect of pFN on bone marrow stromal cells (BMSCs) was examined in the *in vitro* studies.

2. Materials and methods

2.1. Fabrication of the titanium-ion-plated acrylic implant

An acrylic rod (1.0 mm in diameter and 2.0 mm in length) was ultrasonically cleaned in ethanol and distilled water. The titanium-ion-plating methods were applied, based on our previous study [23]. Briefly, the specimens were placed for 10 min in an ion-plating apparatus (MODEL 1602EB; Ayers Rock Corp., Kanagawa, Japan) and were exposed to an argon gas plasma created under 100 W radio frequency power, 12–16 mPa argon gas pressure and 500 V bias voltage. The thickness of the plated titanium was fixed to approximately 20 nm and was confirmed by a cross-sectional transmission electron microscope (JEM 3010; JEOL) at an accelerating voltage of 300 kV.

2.2. Surgical procedures

Ddy mice (8-week-old males, $n = 3$) were anesthetized, a round bone defect 1.0 mm in diameter was created in the middle portion of the diaphysis of the left femur and the implants were inserted. The following two types of implants were used in the experiment:

1. *Ti-acryl* (control group): titanium-ion-plated acrylic implant;
2. *FN-Ti-acryl* (experimental group): titanium-ion-plated acrylic implant soaked in mouse plasma fibronectin (Biogenesis; concentration: 100 μg/ml) at 4 °C for 30 min.

The animals were sacrificed at 1–5, 7 and 14 days after the operation, the samples were perfusion-fixed with 4% paraformaldehyde (PFA) in phosphate-buffered saline (PBS), decalcified with 10% ethylenediaminotetraacetic acid and embedded in paraffin, and thin paraffin sections were prepared (thickness: 3 μm). The sections were first observed histologically with hematoxylin and eosin (H&E) staining.

Animal care and experimental procedures were performed in accordance with the Guidelines for Animal Experimentation of Nagasaki University with the approval of the Institutional Animal Care and Use Committee.

2.3. Immunofluorescence staining and ISH

For the immunofluorescence staining, we prepared a rabbit anti-human pFN antibody according to the methods of Weiss et al. [24]. Additionally, as a marker for the fibroblastic cells, we used goat anti-human cFN antibody (C-20; Santa Cruz Biotechnology). The deparaffinized sections were first blocked with 1% bovine serum albumin (BSA) in PBS for 30 min at room temperature. The slides were incubated with the two primary antibodies diluted with PBS (1:200) for 2 h at room temperature. After extensive washing with PBS, they were incubated with anti-rabbit fluorescein-linked whole antibody (GE Healthcare) and anti-goat Alexa Fluor 594 (Molecular Probe). The fluorescence signals were visualized using a confocal laser microscope (LSM5 PASCAL; Carl Zeiss).

ISH was performed for both groups at day 4 in order to observe the osteogenic activity at the implant surface. For the probe preparation, the cDNAs of osteocalcin (Ocn) subcloned into pGEM-T Easy (Promega) were labeled with digoxigenin with either T7 or Sp6 RNA polymerase. The ISH was performed as described in our previous studies [25].

2.4. Histomorphometrical analysis

The area of the implant surface that was in contact with bone (bone-implant contact, BIC) was calculated at days 5–14. The percentages of bone in direct contact to the implant surface were determined.

The number of fibroblastic cells infiltrated around the implant was counted in a prescribed rectangular area for both groups (0.5 mm × 1.0 mm, adjacent to the implant surface).

Histomorphometric analysis was performed on all specimens using an image analyzing software (Image J ver.1.36b; National Institutes of Health).

2.5. Immunohistochemistry

The proliferation activity of the fibroblastic cells around the implant at day 2 was analyzed by immunostaining the proliferating cell nuclear antigen (PCNA). After preincubation with 1% H_2O_2 in methanol for 30 min, and blocking with 1% BSA, the sections were incubated for 2 h at room temperature with a 1:200 dilution of anti-PCNA antibody (PC10; DAKO). The sections were then incubated with the appropriate biotinylated secondary antibodies, followed by incubation with the avidin–biotin peroxidase complex (Vectastain Elite ABC kit; Vector). The peroxidase conjugates were subsequently localized using diaminobenzidine tetrahydrochloride as a substrate. The ratio of PCNA + fibroblastic cells among all fibroblastic cells was calculated in a prescribed rectangular area (0.5 mm × 1.0 mm, adjacent to the implant surface).

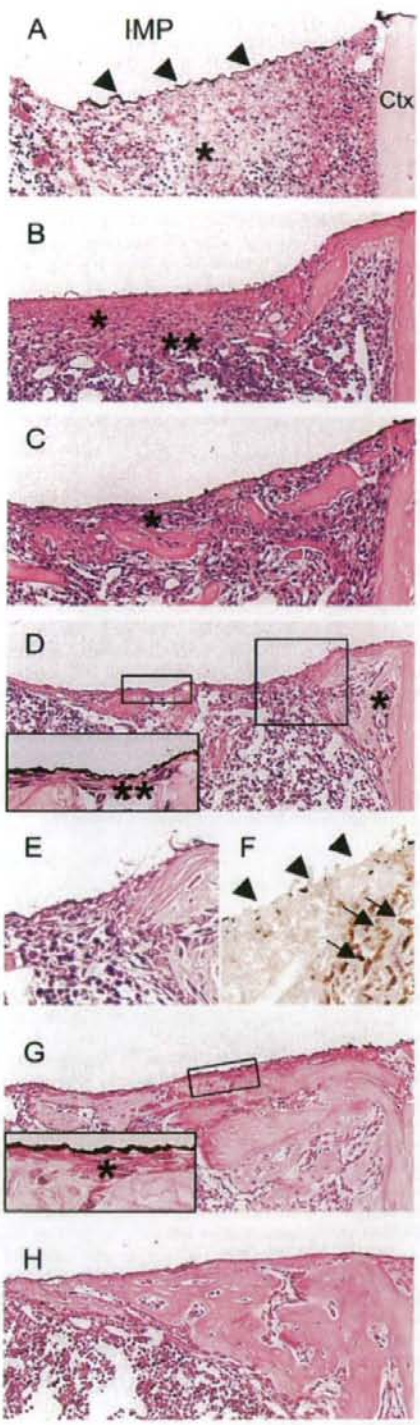

2.6. Preparation of bone marrow stromal cells

The femurs and tibiae of the 8-week-old male ddy mice were cut at the epiphyses, and a BMSCs-rich fraction was obtained by flushing the diaphyseal channel with alpha-MEM (Gibco Laboratories) containing 10% fetal calf serum, 100 μg/ml penicillin G and 100 IU/ml streptomycin through a 23-gauge needle. The cells were then filtrated with a 70-μm nylon filter (Cell Strainer; BD Bioscience), and cultured for 3 days in alpha-MEM containing 10% FCS and antibiotics at 37 °C in 5% CO_2. After 3 days of primary culturing, the non-adherent population was aspirated and the adherent cells were collected by scraping with a rubber wiper; the adherent cells were then concentrated by centrifugation at 1500 revolutions per minute (rpm) for 5 min at room temperature and resuspended.

2.7. Chemotaxis assay

To examine whether or not pFN induces the chemotaxis of BMSCs, the chemotactic responses were measured by means of a modified Boyden chamber assay, using a 24-well-type chamber equipped with polycarbonate filters having 8-μm pores (Chemotaxicell-24; Kurabo, Kurashiki, Japan). The lower side of the filter was coated with either pFN or type-I collagen (CoII; Cell Matrix, Nitta-Gelatin, Osaka, Japan) for 30 min at room temperature within a wide concentration range (from 100 ng/ml to 100 μg/ml). A non-coated filter was used as a control. The lower wells were filled with 600 μl of alpha-MEM, and the upper wells were filled with the obtained cells (40×10^4 cells/ml) in 200 μl of medium. After 24 h of incubation, the filters were carefully removed and the non-migrating cells on the upper side were eliminated by gentle scraping with a rubber wiper and rinsing with cold PBS. The migrating cells on the lower side of the filter were fixed with PFA and stained with toluidine blue. The number of migrating cells was counted at 10 × magnification, and the procedure was repeated in triplicate.

2.8. In vitro proliferation assay

The cellular proliferation activity was estimated based on the uptake of bromo-deoxyuridine (BrdU). Polystyrene 96-well plates were coated with pFN (concentration: from 100 ng/ml to 100 μg/ml) at 4 °C for 30 min. The wells were then blocked with 1% BSA for 30 min at room temperature and rinsed with PBS before adding the cells. As a control, CoII-coated wells with the same concentration range and non-treated wells were used. The cells were then added (40×10^4 cells/ml) and cultured for 24 h. Cell viability was assessed by the Biotrak™ cell proliferation ELISA system (GE Healthcare), according to the manufacturer's instructions.

Fig. 1. Histological analysis of the Ti-acryl group. Hematoxylin/eosin (H&E) stainings of decalcified bone sections. The original magnification is 10× (A–D and G–H). (A) Day 1: titanium film is still present at the tissue–implant interface (arrowheads). Edematous peri-implant tissue (asterisk). IMP: implant; Ctx: cortex. (B) Day 2: fibrinous layer at the implant surface (asterisk). The infiltration of fibroblastic cells away from the implant surface (double asterisk). (C) Day 3: direct infiltration of the fibroblastic cells to the implant surface (asterisk). (D) Day 4: new bone formation observed underneath the cortex (asterisk). Higher-magnification image of the tissue–implant interface (inset: original magnification 40 ×). Fibroblastic cell infiltration can be observed at the implant surface (double asterisk). (E) Higher magnification of the initial bone formation underneath the cortex at day 4 (original magnification 40 ×). (F) ISH for Ocn mRNA expression. Ocn mRNA could not be detected at the implant surface (arrowheads). On the other hand, Ocn mRNA was expressed away from the implant surface (arrows). (G) Day 5: the inset shows a magnified image (original magnification 40 ×). Fibroblastic cell infiltration can still be seen at the implant surface (asterisk). Note that there is no direct bone–implant contact. (H) Day 7: direct bone–implant contact can be seen.

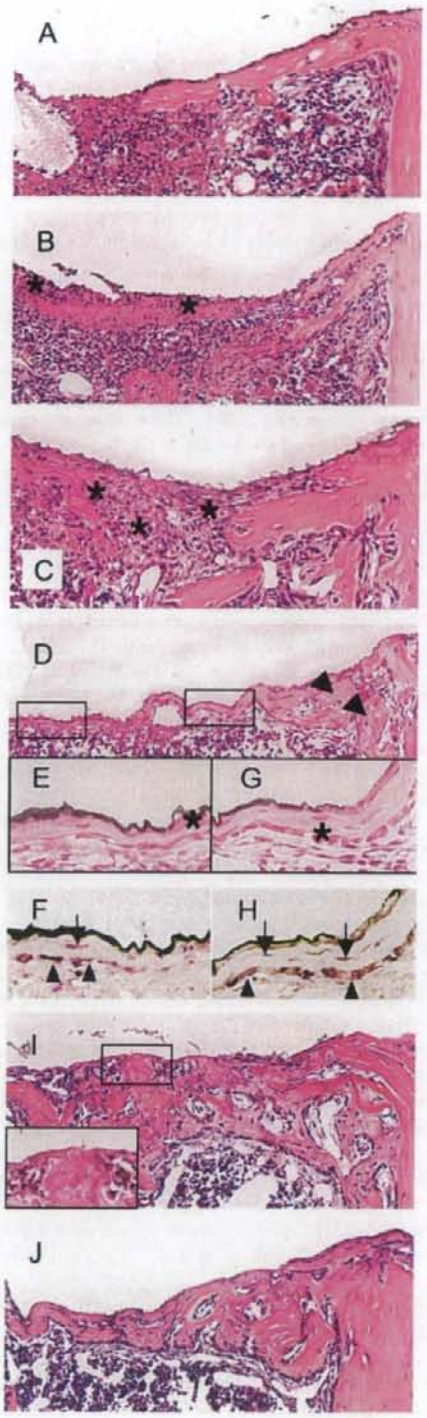

2.9. Analysis of osteogenic differentiation in vitro

In order to assess the osteoinductive role of pFN, BMSCs-rich fractions were cultured on pFN- or Coll-coated or non-coated dishes and transfected with adenoviral rh-BMP-2 [26]. After 4 days, the transfection-elevated alkaline phosphatase (ALP) production was compared among the three groups. The ALP activity was detected by enzyme histochemistry, as in our previous studies [27].

2.10. Statistical analysis

All statistical analyses in this study were performed with KaleidaGraph (Synergy Software). The mean and standard deviation values of the histomorphometric and *in vitro* parameters ($n = 3$) were calculated. The average values were compared by one-way analysis of variance, followed by a *post hoc* Tukey test with the value of statistical significance set at the 0.05 level.

3. Results

3.1. Histological examination of the bone formation process for Ti-acryl and FN-Ti-acryl

In the Ti-acryl (control) group, the peri-implant bone healing proceeded as follows. At day 1, the peri-implant tissue was edematous (Fig. 1A). At day 2, a dense fibrin layer was observed just outside of the implant surface; sparse infiltration of spindle-shaped fibroblastic cells was noticed outside of the fibrin layer (Fig. 1B). At day 3, the fibroblastic cells surrounded the implant surface (Fig. 1C). At day 4, new bone formation was seen in an area hemmed by the cortex and the implant; however, bone formation could not be observed at the implant surface; mononuclear cells or fibroblastic cells surrounded the surface of the implant (Figs. 1D and E); no expression of Ocn mRNA was observed at the implant surface (Fig. 1F). At day 5, the bone volume increased; however, layers of fibroblastic cells were still observed at the implant surface (Fig. 1G). At day 7, the bone volume increased further and at last, the bone was in direct contact with the implant surface (Fig. 1H). At day 14, the bone volume increased even further and the bone became compact (data not shown).

Whereas, in the FN-Ti-acryl (experimental) group, at day 1 the peri-implant tissue was less edematous than in the control group (Fig. 2A). At day 2, fibroblastic cells reached

Fig. 2. Histological analysis of the FN-Ti-acryl group. H&E staining of decalcified bone sections. The original magnification is 10 × (A–D and G–H). (A) Day 1: the peri-implant tissue was dense and less edematous than that shown in Fig. 1A. IMP: implant; Ctx: cortex. (B) Day 2: direct fibroblastic cell infiltration to the implant surface (asterisks). (C) Day 3: further infiltration of fibroblastic cells (asterisk). (D) Day 4: new bone formation underneath the cortex (arrowheads). Higher magnification of the bone–implant interface at day 4 (E–H: original magnification is 40 ×). (E and G) H&E stainings. The deposition of bone matrix adjacent to the implant surface (asterisk). (F and H) ISH analysis of the bone–implant interface. Note that Ocn mRNA expression was detected in the cells inside the bone matrix (arrows) and in the cells rimming the bone matrix (arrowheads). (I) Day 5: direct bone–implant contact can be seen (inset). (J) Day 7: the bone volume further increased and the bone became compact.

the implant surface and infiltrated the surrounding tissues (Fig. 2B). At day 3, a larger number of fibroblastic cells infiltrated the area around the implant compared to the Ti-acryl group (Fig. 2C). At day 4, deposition of bone matrix appeared directly on the implant surface, as well in an area hemmed by the cortex and the implant (Fig. 2D); osteoblastic cells rimming the matrix and osteocytic cells embedded in the matrix were observed under higher magnification (Figs. 2E and G); Ocn mRNA expression was detected in the cells at the bone–implant interface and in the bone matrix (Figs. 2F and H). At day 5, the bone matrix was in direct contacted with the implant surface, without the intervention of any fibroblastic cells at the bone–implant interface, and the bone volume around the implant increased (Fig. 2I). At days 7 (Fig. 2J) to 14 (data not shown), the bone volume further increased and the bone became compact.

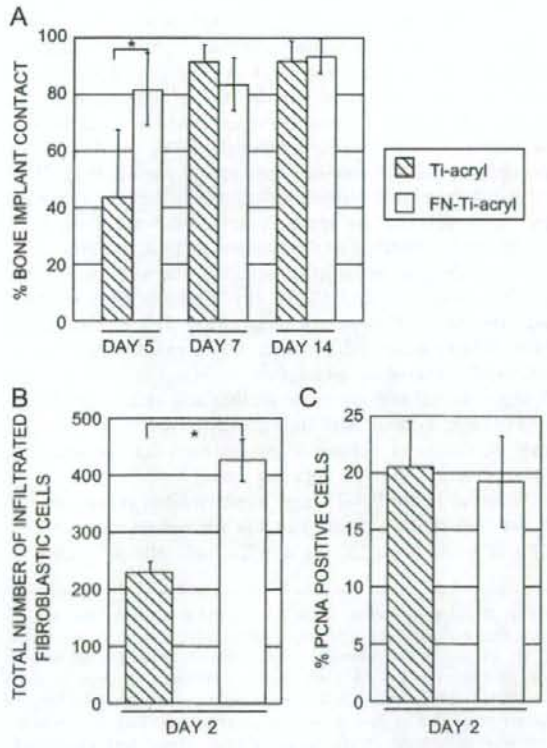

Fig. 3. Histomorphometrical analysis. (A) The percentages of bone in direct contact with the implant in the two groups were determined at days 5–14. The BIC was significantly higher in the experimental group at day 5. (B) The number of infiltrated fibroblastic cells was significantly higher (1.86 times) in the experimental group at day 2. (C) No significant difference in the proliferation activity was observed between the two groups at day 2. The values represent means ± SD of five separate experiments performed in triplicate ($*p < 0.05$).

3.2. BIC analysis

The BIC in the experimental group was significantly higher than those in the control group at day 5. In the control group, the BIC was 43.6% and in the experimental group, the BIC was 81.6%. There was no significant difference between the BIC values of these groups at days 7 and 14 (Figs. 3A and B).

3.3. Infiltration of fibroblastic cells and PCNA proliferation assay

The total number of infiltrated fibroblastic cells in the experimental group was 1.86 times larger than that in the control group (Fig. 3C). The percentage of PCNA + fibroblastic cells at day 2 was 20.5% in the control group and 19.2% in the experimental group (Fig. 3D). There was no significant difference in the proliferation rates of the two groups.

3.4. Immunofluorescence staining

In the control group at day 1, pFN signals were detected, not around the entire implant surface, but chiefly in an area hemmed by the cortex and the implant (Fig. 4A). At day 2, the pFN signals disappeared at the implant surface, whereas they could still be detected in the matrix away from the implant surface (Figs. 4B–D). Strong cFN signals were detected in the fibroblastic cells; however, lower pFN signals were detected at the implant surface compared to the matrix away from the implant (Figs. 4C, E and F). The corresponding H&E stained sections show an infiltration of fibroblastic cells outside of the fibrin layer (Fig. 4G). At day 3, the pFN signals were drastically reduced (Fig. 4H) and the infiltration of cFN-negative fibroblastic cells could be seen at the implant surface (Figs. 4I–K). At day 4, both signals completely disappeared (data not shown).

In the experimental group at day 1, pFN immunofluorescence signals were detected extensively around the implant surface and in the surrounding matrix (Fig. 5A). At day 2, the pFN signals were still observable at the implant surface (Figs. 5B–E); cellular-FN + fibroblastic cells also reached the implant surface and infiltrated the surrounding matrix (Figs. 5C, E and F). The corresponding H&E sections show a direct infiltration of fibroblastic cells to the implant surface (Fig. 5G). At day 3, capillaries were generated in some places adjacent to the implant surface; the infiltration of cFN + fibroblastic cells was also evident in this area (Figs. 5I–K), while pFN signals around the implant decreased (Fig. 5H). At day 4, both signals were still visible, but lower compared to those at day 3 (data not shown).

3.5. Effect of pFN on the chemotaxis, proliferation and osteo-differentiation of BMSCs

The chemotaxis assay revealed that pFN significantly promoted the chemotaxis of BMSCs compared to the ColI-coated or non-coated chambers (Fig. 6A). Although the

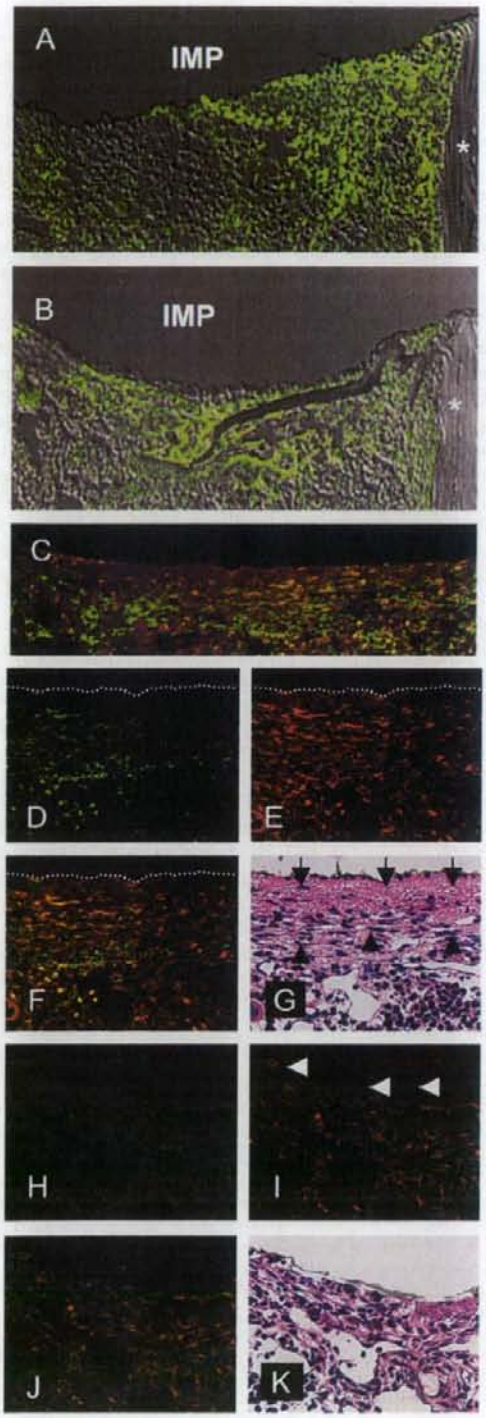

chemotactic activity of BMSCs increased in a dose-dependent manner in both the pFN and the ColI-coated group, the chemotactic ratio in the pFN-coated group was significantly higher than that in the ColI-coated group at all concentrations tested. The BrdU-uptake of BMSCs cultured on the various groups of wells did not result in any significant differences in proliferation ratio (Fig. 6B). The histochemical analysis of the ALP enzyme revealed no drastic variance in ALP activity between any of the cells cultured on any well after the transfection of BMP-2 (Fig. 6C).

4. Discussion

This is the first report that addressed the *in vivo* localization and role of pFN during osseointegration. Our results demonstrated that coating the implant with pFN induced faster osseointegration compared to the non-coated implant, and suggested that this phenomenon was due to the recruitment of larger number of cFN + BMSCs closer to the implant surface by the preferential chemotactic activity of pFN. Although the adsorption of blood proteins to the titanium implant has been suggested to play an important role for osseointegration [7,28], the actual *in vivo* localization of blood proteins and its role for osseointegration remained uncertain. In this study, we developed the paraffin-sectionable titanium ion-plated acrylic implant model for the detection of *in situ* localization of molecules involved in osseointegration. The paraffin sections showed titanium film attached directly to the peri-implant tissue, meaning the bone–implant or tissue–implant interface was well preserved.

During days 2–3, there was a drastic reduction of the pFN signal in the control group. In contrast, the pFN signal could still be detected at the implant surface in the experimental group. The pFN detected in the experimental group may be due to the release of pFN from the pFN-coated implant. The histological results of this study show that, at day 2, the infiltration of a larger number of cFN + BMSCs to the implant surface could be observed in the experimental group compared to the control group (Fig. 3C). At day 3, the infiltration of cFN + BMSCs to the implant surface was evident only in the experimental group, and the cells which reached the implant surface in the control group were cFN-negative (Figs. 4I, K and 5I, K).

Fig. 4. Localization of pFN (green) and cFN (red) for the Ti-acryl group. IMP: implant; asterisk: cortex. Immunofluorescence image of pFN with a differential interference image of peri-Ti-acryl tissue at day 1 (A) and day 2 (B). The original magnification is 10×. (C) Merged image of the tissue–implant interface at day 2. The original magnification is 20×. (D and H) Localization of pFN (D, day 2; H, day 3). (E and I) Localization of cFN (E, day 2; I, day 3). Note that the cells infiltrated near the implant surface are cFN-negative (I; arrowheads). (F and J) Merged image of pFN and cFN at the implant surface (F, day 2; J, day 3). The same section field stained with H&E (G, day 2; arrows: fibrin layer, arrowheads: fibroblastic cells; K, day 3). The dotted lines (D–F) trace the tissue–implant interface. The original magnification is 40× for D–K.